RSC Advances

PAPER

View Article Online
View Journal | View Issue

Cite this: RSC Adv., 2016, 6, 37424

Influence of morphology on the performance of ZnO-based dye-sensitized solar cells†

F. I. Lizama-Tzec,[a] R. García-Rodríguez,[a] G. Rodríguez-Gattorno,[a] E. J. Canto-Aguilar,[a] A. G. Vega-Poot,[a] B. E. Heredia-Cervera,[a] J. Villanueva-Cab,[b] N. Morales-Flores,[c] U. Pal[b] and G. Oskam*[a]

ZnO nanomaterials with different morphologies, obtained by a sonochemical synthesis method at pH values of 5.5, 8, 10 and 12, have been used as starting materials for the fabrication of dye-sensitized solar cells. The morphology of the nanomaterials and the texture of the films deposited using screen printing depend on the synthesis pH, and the various exposed surface facets interact in a different manner with the dye and electrolyte solutions. The best cell performance was obtained with the morphology that resulted from the synthesis at pH 10, where the {100} and {110} crystal forms are predominant, and where dye coverage was largest. Interestingly, the BET total surface area was lowest for this nanomaterial illustrating the importance of morphology. The influence of the synthesis pH was also evident in the energetics and recombination kinetics of the solar cells. For the ZnO material synthesized at pH 5.5, the band edges appear to be shifted to more negative potentials, which could have resulted in a larger open circuit potential based on thermodynamic considerations. However, the electron life time for the pH 5.5 ZnO material is significantly smaller than for the other three synthesis pH values, indicating that the recombination kinetics are significantly faster for these cells as well, resulting in a smaller open circuit potential based on kinetics arguments. The balance between these two effects determines the experimentally observed open circuit potential. Overall, the results indicate that the dependence of the dye adsorption characteristics on ZnO nanomaterial morphology and film texture are the dominating factors that determine the solar cell performance.

Received 2nd December 2015
Accepted 6th April 2016

DOI: 10.1039/c5ra25618f

www.rsc.org/advances

1. Introduction

The dye-sensitized solar cell (DSSC) is a promising candidate for a variety of applications related to the use of abundant materials, a low manufacturing cost, and specific niche features, such as a superior performance in conditions of low intensity, low angle of incidence and high temperature as compared to silicon solar cells.[1] The DSSC has also been marketed for its high efficiency under indoor lighting. DSSCs are typically based on titanium dioxide (TiO_2); however, zinc oxide (ZnO) is an interesting alternative to TiO_2 because it is a versatile material, with potentially better electrical properties.[2,3] While the energetics of ZnO and TiO_2 in terms of band gap and band positions are very similar, the electron mobility in bulk ZnO is higher than for TiO_2, which could lead to a higher electron collection efficiency. However, ZnO-based cells have not reached the efficiency of the best TiO_2 devices, which is due to generally faster recombination[3] and less-favourable interfacial energy level alignment or lower injection efficiency.[4–8] ZnO is a material that is easy to synthesize in a large variety of morphologies and by a multitude of methods. In addition, it is possible to deposit crystalline ZnO at low temperatures, making it very suitable for deposition onto plastic flexible substrates.[9–23]

The properties of the ZnO/dye/electrolyte interface are expected to depend on the surface chemistry of the facets exposed, including the surface acidity and electron density, which may significantly affect dye adsorption, energy level alignment, injection kinetics as well as recombination kinetics. For example, the (100) and (110) planes are both terminated in Zn and O, while the (101) plane is oxygen-terminated,[24] which could affect all of the above properties. The interaction of dyes with semiconductor surfaces is a chemical process that is strongly correlated to local acidity of the facet, therefore, preferential growth and texture of nano/micro particles are parameters that can be exploited to improve the performance of DSSC devices.[25,26] In the present work, we relate the morphology and texture of ZnO nanomaterials prepared by sonochemical

[a]Department of Applied Physics, CINVESTAV-IPN, Mérida, Yuc. 97310, México. E-mail: gerko.oskam@cinvestav.mx

[b]Instituto de Física, Benemérita Universidad Autónoma de Puebla, Puebla, Pue. 72570, México

[c]Centro de Investigación en Dispositivos Semiconductores, ICUAP, Benemérita Universidad Autónoma de Puebla, Puebla, Pue. 72570, México

† Electronic supplementary information (ESI) available. See DOI: 10.1039/c5ra25618f

synthesis as a function of the pH to the performance of ZnO-based DSSCs.

2. Experimental

2.1 ZnO powders with different morphologies

ZnO with different morphologies were synthesized using a sonochemical method reported previously.[23] For this purpose, a 68 mM zinc acetate solution was prepared by dissolving 3 g of zinc acetate dihydrate [$Zn(C_2H_3O_2)_2 \cdot 2H_2O$, Baker, 99.9%] in 200 ml of deionized water (DI) at room temperature with vigorous stirring. Then an appropriate amount of ammonium hydroxide (NH_4OH) was slowly added to the solution until the pH of the mixture reached a desired value. The resulting solution was kept with ultrasonic agitation using a Ti ultrasonic processor (UP400S, Hielscher, 400 Watt, 24 kHz) at 40 W dissipated power under argon gas flow for 3 h. Finally, the obtained product was centrifuged and washed several times with ethanol and dried at 70 °C for 6 hours. Distinct morphologies were obtained by adjusting the pH of the synthesis to the following values: 5.5, 8, 10 and 12.

2.2 Preparation of a ZnO screen printing paste

A viscous screen printing paste was prepared by dispersing ZnO powder in ethanol (J.T. Baker 99.9%), maintaining a ratio of 0.5 g of ZnO in 10 ml of ethanol. Ethylcellulose was dissolved (Aldrich, viscosity 100 cP, 48% ethoxyl) in ethanol to obtain a final proportion of 30% with respect to the ZnO content. In order to balance the viscoelastic properties of the final paste, 4.06 g terpineol (mixture of isomers, anhydrous, Aldrich 99.5%) was added to the ZnO dispersion. After mixing with terpineol, the suspension was concentrated to a paste by evaporation of ethanol using a rotary evaporator (Büchi, R-210). This process was repeated for each ZnO powder. This screen printing paste composition gave an average porosity of 53% for the deposited films.

2.3 Porous ZnO layers by screen printing

The screen printing method is capable of producing level layers reproducibly even for large areas, and this method is typically used to fabricate DSSC panels.[27,28] After obtaining the paste, ZnO layers were deposited on previously cleaned fluorine-doped tin oxide (FTO, TEC 15 Pilkington) coated glass with an application area of 0.5 cm^2. Screen printing was performed by sliding the squeegee at an 80° angle over the screen. Between applications, the substrate was placed for 6 minutes on a hot plate at 125 °C. The approximate film thickness was 1.1 ± 0.2 μm per application. After application of all layers, the films were sintered at 450 °C for 1 hour, and after cooling down they were treated with aqueous H_2SO_4 at pH 2.2. After the acid treatment, the films were sintered again at 450 °C for 1 hour. After this second step, the layers were allowed to cool slowly to 90 °C and were sensitized with the N-719 dye (Ruthenium 535-bis TBA; Solaronix) by immersion in a 0.5 mM dye solution in ethanol for 2.5 hours. The amount of dye adsorbed was determined using UV-Vis spectrophotometry by desorbing sensitized films in 3 ml of a 10 mM NaOH solution, and calculating the number of moles of dye molecules from a calibration curve. The density of adsorbed dye was determined by dividing by the total surface area, which was determined by multiplying the BET surface area with the weight of the films obtained by scraping off the films after dye desorption and drying.

2.4 ZnO film characterization

After deposition, the ZnO film thickness was measured by profilometry (D-120; KLA-Tencor). The specific surface area of the ZnO film material was determined using nitrogen adsorption–desorption isotherms at 77 K (Belsorp-Mini II; BEL Japan). Before recording the isotherms, the samples were degassed at 250 °C for 5 hours in vacuum. The morphology and texture ZnO films were studied by scanning electron microscopy (SEM; JEOL JSM-7600F) and X-ray diffraction (XRD-5000; Siemens) with monochromatic CuKα radiation, $\lambda = 1.54$ Å, operating at 40 kV and 40 mA. Miller's notation was used to describe morphological and crystal structure relationships. The wetting characteristics were tested by applying a water drop to freshly prepared ZnO films after the sintering steps: the contact angle was found to be independent of ZnO material at 18–20°, hence, the films are hydrophilic.

2.5 DSSC assembly and characterization

Solar cells were assembled in a sandwich structure of the FTO/ZnO/dye working electrode and platinum-catalyzed FTO counter electrode, separated by a 60 μm Surlyn polymer sealant (DuPont). After sealing, the cell was filled with the electrolyte solution through small holes previously perforated in the counter electrode. The electrolyte solution consisted of 0.6 M DMPII (1,2-dimethyl-3-propylimidazolium iodide), 0.1 M LiI (lithium iodide), 0.1 M GuSCN (guanidine thiocyanate), 50 mM I_2, and 0.5 M 4-*tert*-butylpyridine in acetonitrile–valeronitrile (85 : 15 v/v%). The cell efficiency was determined using a calibrated Xenon lamp (Oriel) at 1 sun (100 mW cm^{-2}). The system was calibrated by adjusting the light intensity using the AM 1.5 G filter in combination with a Schott KG5 filter.

2.6 Electrochemical spectroscopy (EIS) and current–voltage characterization

The impedance spectra and the current–voltage curves were measured with an Autolab PGSTAT302N/FRA2 set up. The AC signal amplitude was 10 mV and the frequency range was 100 kHz to 0.01 Hz. The impedance spectra were analyzed using the Zview modeling software from Scribner Associates with the aid of a transmission line equivalent circuit shown in Fig. 1.[29,30] For EIS measurements under illumination a high intensity Luxeon red LED (625 nm) illumination source was used. In Fig. 1, R_S represents the series resistance; R_{FTO} and C_{FTO} stand for the elements of resistance and capacitance for the recombination *via* the FTO substrate not covered by the ZnO nanoparticles; R_{tr} represents the resistance for electron transport along the metal oxide nanoparticles; R_{ct} is the charge transfer resistance related to the process of recombination between electrons in the metal oxide and the redox species in the electrolyte solution; C_μ is the

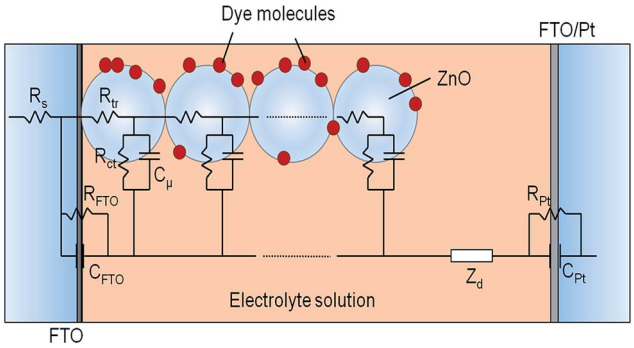

Fig. 1 General equivalent circuit model used to fit impedance spectroscopy spectra for DSSCs.

chemical capacitance for charge accumulation in the metal oxide particles; Z_d is the Warburg impedance of the diffusion of the redox species in the electrolytic solution; R_{Pt} stands for the charge transfer resistance at the counter electrode/electrolyte interface and C_{Pt} represents the interfacial capacitance at the counter electrode/electrolyte interface.

3. Results

3.1 Characterization ZnO powder

In Fig. 2 the X-ray diffraction patterns of ZnO powders obtained by sonochemical synthesis at different pH values are shown. In all samples, the reflections are consistent with the database pattern JCPDS No. 36-1451, which corresponds to ZnO in the wurtzite phase crystallized in the hexagonal structure with spatial group $P6_3mc$ (No. 186).[31]

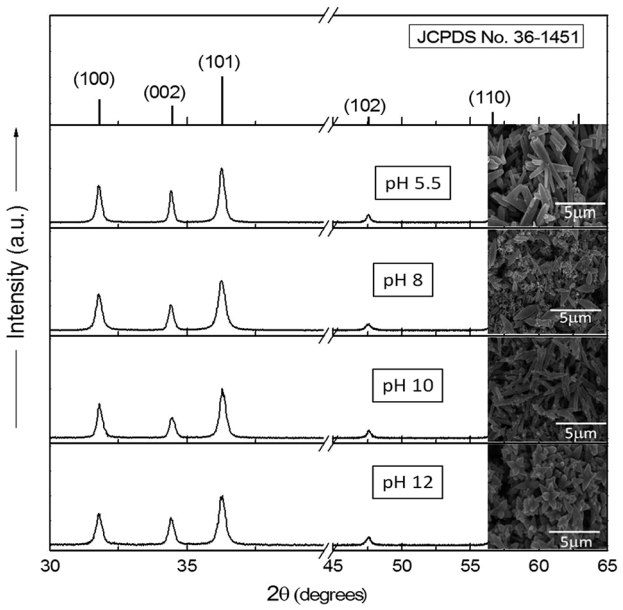

Fig. 2 XRD patterns of ZnO powders normalized with respect to the (101) plane. On the right hand side, selected SEM images of ZnO synthesized at different pH values are shown. The axis break covers a range where no reflections were observed. The top graph shows the corresponding reference pattern.

The influence of nanoparticle size on solar cell efficiency can be generalized to be dominated by two effects: (i) total surface area of the film; and (ii) inter-particle electrical connectivity. The first effect relates the surface area with the number of active sites available for surface interaction, for example, (a) dye adsorption; or (b) charge transfer to the solution, which in this case corresponds to recombination in the solar cell. The second effect (ii) mainly relates to the electron transport process in the nanostructured film. The full-width at half-maximum (FWHM) values of the peaks are small, indicating well-crystallized products and relatively large crystallite size. Formation of $Zn(OH)_2$ is not detected by X-ray diffraction. The lack of an inversion center in the ZnO crystal structure results in the existence of polar and non-polar surfaces, where the polar surfaces are related with the {001} family of planes while the non-polar surfaces correspond to the crystallographically equivalent families {100} and {110}. The polar surfaces (perpendicular to the *c* axis) are terminated in zinc cations or oxygen anions, hence zinc-terminated surfaces tend to be positively charged and interact with negative species in solution while the opposite occurs for oxygen-terminated surfaces. On the other hand, the non-polar surfaces are three-fold coordinated zinc and oxygen terminated surfaces that can act simultaneously as Lewis acid and base sites. The SEM images in Fig. 2 show that the material has a tendency to form elongated microstructures. Two important features arise when the morphology is explored in detail: the first is a clear increase in the number of multiple twinned particles at high pH value (star-like morphology with sharp-pointed ends), and the second is the predominance of rods with sharpened ends with an angle between the terminating surfaces that diminishes from pH = 8 toward pH = 10 and increases at pH = 12.

If the intensities of the experimental X-ray diffraction patterns are compared with those expected (without preferred orientation), a preferential growth along the ⟨002⟩ axis direction can be observed (see Section 3.3), which is consistent with the observed elongated morphology in the SEM micrographs. The observed growth habit modifications as function of the pH are related to differences in relative growth rates at crystal faces, which depend on the relative chemical interactions of ions (or molecules) with the ZnO surfaces during the synthesis processes. In general, the influence of the experimental conditions on the morphology of ZnO in solution-phase synthesis has been studied previously, and our observations are consistent with previous studies.[33–36] Elongation along the ⟨002⟩ direction is a well-documented behavior of ZnO in solution synthesis,[37–40] which results from the adsorption of chemical species on {010} and {011} surfaces. In acidic conditions, the morphology of ZnO can give rise to flat-top rods,[41] on the other hand, at higher pH it is also well established that OH^- anions block the {002} polar surfaces allowing the enhanced presence of higher index surfaces such as {011} that give the sharp-pointed ends shape to the crystals.[42] Fig. 3 shows a schematic representation of the main morphological features as function of the synthesis pH. The image on the top shows the principal planes and their relation with the main surface facets involved; note here that the planes belonging to the {010} and {011} families define the

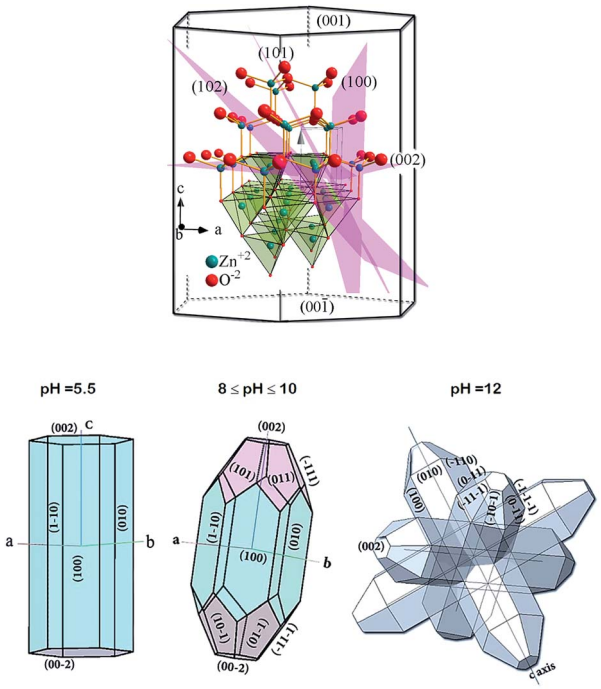

Fig. 3 Schematic representation of the ZnO morphology for each synthesis pH. The scheme in the top image illustrates the relationship between main planes and surfaces. The particle habit was simulated using Crystal Shaper software version 1.3.1 following the Donnay–Harker methodology.[32]

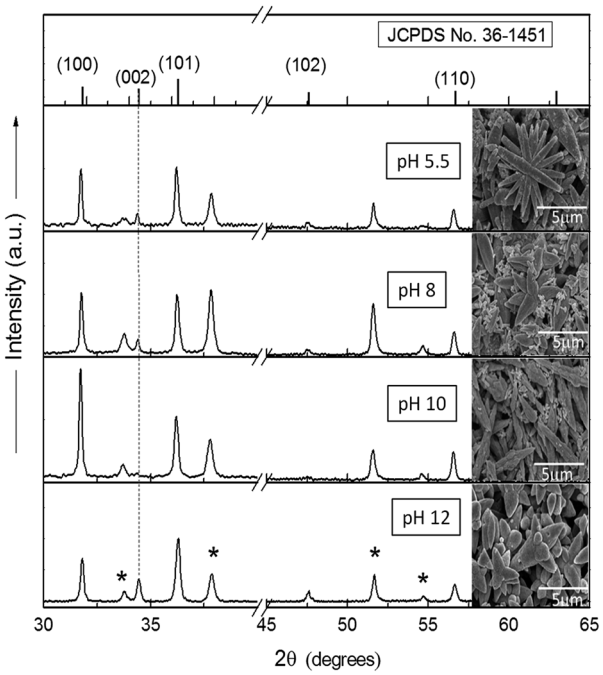

Fig. 4 XRD patterns of ZnO films on FTO normalized with respect to the (101) plane. The SEM micrographs of ZnO obtained at different pH values are shown on the right. The asterisk corresponds to reflections of fluor-doped tin oxide (FTO) from the transparent conducting substrate. The axis break covers a range where no reflections were observed.

sharp-pointed form of the microrod ends. According to SEM observations, multi-twinning in star-like particles occurs at an angle of 60° or 90° depending on the number of branches (6 or 4 around a central rod), revealing that the basic symmetry elements belong to the spatial group of the wurtzite crystal.

3.2 Characterization ZnO films

Mesoporous, nanostructured ZnO films were prepared by screen printing, and the thickness, surface area, texture and morphology of the films were determined. Fig. 4 shows the XRD patterns for the ZnO films deposited onto FTO using the powders obtained at different pH. The high degree of texturing of the material can be clearly observed in all films, where the sharp decline in the intensity of the (002) plane reflection indicates that the ⟨002⟩ axis runs nearly parallel to substrate surface. The texturing of rod-shaped particles is related to the use of the screen printing method to deposit the films. The screen printing method is based on the rheological properties of the ZnO paste. As the paste is squeezed through the screen, the viscosity of the paste reaches a minimum value due to the thixotropic properties of the cellulose used in the formulation of this paste. Hence, during this process the mobility (axial and radial rotation) of ZnO rods increases, allowing for the arrangement of particles with their main axes parallel to each other. Immediately after the paste is deposited onto the substrate, it recovers its high viscosity thus impeding the motion of particles and further rearrangement. Finally, during the heat treatment, the particles consolidate with a texture where the texture coefficient reduction suggests that most of particles are nearly parallel to the substrate surface. The micrographs on the right hand side of Fig. 4 show selected SEM images for the ZnO films: it can be seen that the morphology remains essentially unchanged, which suggests that the deposition process does not significantly affect the particle size and surface facet distribution.

3.3 Morphology and texture

With the aim of describing the trend of the preferred orientation of the different powders and comparing with texturing after film deposition, the Harris' texture coefficient TC(*hkl*) was calculated as follows:

$$\mathrm{TC}(hkl) = \frac{I(hkl)/I_0(hkl)}{\frac{1}{n}\sum_{j=1}^{n} I(hkl)/I_0(hkl)} \quad (1)$$

where I is the measured intensity, I_0 the JCPDS standard intensity (used for the case of powders) or the absolute intensity of the reflections for the corresponding powder (for the case of the films) and n the number of diffraction peaks. The TC value ranges from 1 (no texture) to N (for oriented crystals compared with a reference). In the intensity profiles from XRD there is implicitly an overlap of the information on morphology, which we define as preferential orientation within a microcrystal, and texture, which refers to the relative organization of microcrystals with respect to each other and their relative angle with respect to substrate surface. Fig. 5 shows the obtained TC(*hkl*)

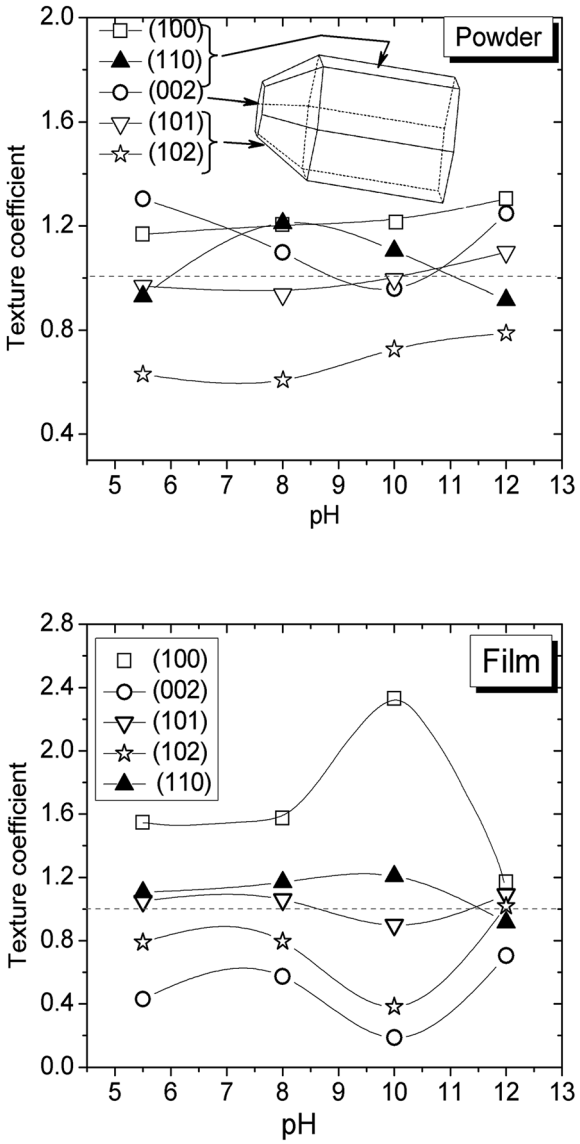

Fig. 5 Variation of the texture coefficient TC(*hkl*) of ZnO obtained at different pH values. The graph at the top corresponds to the starting powders; the graph at the bottom corresponds to films.

values *versus* the synthesis pH, illustrating that for powders (top) the values oscillate around unity only for the (101) reflection in all samples. The increasing value of TC(110) is revealing the flattened nature of the morphology in samples obtained at pH 8 and pH 10, while the preferential orientation ⟨002⟩ for samples obtained at pH 10 reaches a minimum. The trend in texture coefficients shows that the morphology features at the extreme pH values (pH 5.5 and 12) are consistent with previous studies.[41,42] Recent studies demonstrate that morphologies with exposed higher-index surfaces allow for better power conversion efficiency with several dyes (including N719) due to higher adsorption energies of these facets.[43] On the other hand, the TC(*hkl*) graphs of the screen printed and sintered ZnO films (Fig. 5, bottom graph) reveal a different trend; since the TC(*hkl*) values were calculated with respect to the intensity of the peaks of the X-ray diffraction pattern of the powder, which minimizes contributions from intrinsic morphology of the particles, the observed features are related to film texturing during the deposition process. In this case, the TC(*hkl*) values corresponding to the multi-twinned morphology obtained at pH 12 are essentially independent of {*hkl*}, which is probably related to its star-like morphology that favors a randomly distributed orientation of planes. The other samples are considerably textured along the ⟨002⟩ axis, especially the film prepared with powder obtained at pH 10. The actual consequences of these texturing behaviors in the performance of the cells are difficult to predict as the accommodation of particles could affect the accessibility of the dye to certain surfaces, the contact between grains, charge transport in the film, and charge transfer at the ZnO–FTO interface. Previous studies have evidenced the anisotropy of fundamental properties such as photoluminescence and Schottky barrier heights for ZnO elongated morphologies,[44–51] both properties connected with charge generation, recombination and transport. On the basis of these reports one can reasonably predict that in elongated polycrystals the charge transport could be favored by the texturing along ⟨002⟩ parallel to surface of the substrate, hence, those cells prepared with powders obtained at pH 8 and 10 could show enhanced performance.

It is important to remember that while the preferential orientation of the powder could influence the surface chemistry affecting the amount of absorbed dye, the texturing of the material over the substrate in the films could affect the charge transport in the film. Table 1 shows a summary of the results. The film thickness is about 10 μm for all materials, however, the specific surface area and porosity are a function of the synthesis pH. The BET specific surface area for the different morphologies synthesized was largest for the sample obtained at pH 5.5, while the other materials have very similar specific surface areas. In order to determine the total surface area, the ZnO films were removed from the FTO substrate after sintering, and the resulting ZnO material was weighed. Interestingly, the smaller amount of ZnO deposited corresponds to the film obtained from the pH 5.5 sample, indicating a significantly higher porosity. The adsorption characteristics of the N719 dye can be evaluated using the results of the total surface area. In last column of Table 1, the quantity of adsorbed dye is shown, which was determined using UV-Vis spectrophotometry: sensitized films were immersed in a known volume of an aqueous NaOH solution at pH 12 in order to desorb the dye, and the absorbance of the corresponding solutions was related to the dye concentration considering a molar extinction coefficient[52,21] at 515 nm of 1.41×10^4 L mol^{-1} cm^{-1}.

It can be seen from Table 1 that there is no clear correlation between total surface area and the amount of dye absorbed, which indicates the relevance of differences in morphology characteristics between the different ZnO materials. The maximum dye coverage is observed for the ZnO obtained at pH 10, which is characterized by the lowest specific and total surface area. It is well-known that dyes interact strongly with polar surfaces [see for example ref. 45], however, in our case the contribution to the total surface area from {001} polar surfaces is expected to be relatively low since in all samples the

Table 1 Characteristics of the ZnO powders and sintered, screen-printed ZnO films. The results represent an average of three sets of films

Synthesis pH value	Film thickness (μm)	Specific surface area ($m^2\ g^{-1}$)	ZnO film weight (mg)	Film surface area ($10^{-3}\ m^2$)	Adsorbed dye (10^{-10} mol cm^{-2})
5.5	9.8	22	0.86	19	2.3
8	10.0	5.0	1.5	7.5	7.7
10	10.2	4.0	1.6	6.4	17
12	10.5	5.0	1.3	6.5	5.6

morphology is elongated with aspect ratio higher than 5; therefore, the main contribution to surface area is provided by lateral surfaces. The unique differences between lateral surfaces is their relative Zn–O density (0.065 $Å^{-2}$ for the {100} and {110} surfaces and 0.056 $Å^{-2}$ for the {101} and {102} surfaces), [see ref. 53]. Therefore, a higher density of {100} and {110} surfaces should imply a higher dye adsorption capability. From Fig. 5 (top), it appears that the ZnO materials obtained at pH 8 and 10 have ideal surface contributions for dye absorption, however, the accommodation of particles in the films (texturing) also appear to play some role in the accessibility of the dye to certain surfaces. As a consequence, in most series of experiments, the results obtained for the materials prepared at pH 8 and pH 10 were quite similar, with pH 10 slightly preferred.

3.4 Characterization of dye-sensitized solar cells

Fig. 6 shows the current–voltage curves for dye-sensitized solar cells based on the ZnO films with different morphologies and the cell parameters are collected in Table 2. There is a clear influence of the ZnO morphology or texturing of the particles in the film on the solar cell performance. For example, the short-circuit photocurrent is lowest for the cell prepared with the ZnO obtained at pH 5.5, which paradoxically has the highest surface area as previously shown in Table 1, and highest for the ZnO synthesized at pH 10, which has the lowest specific and total surface area.

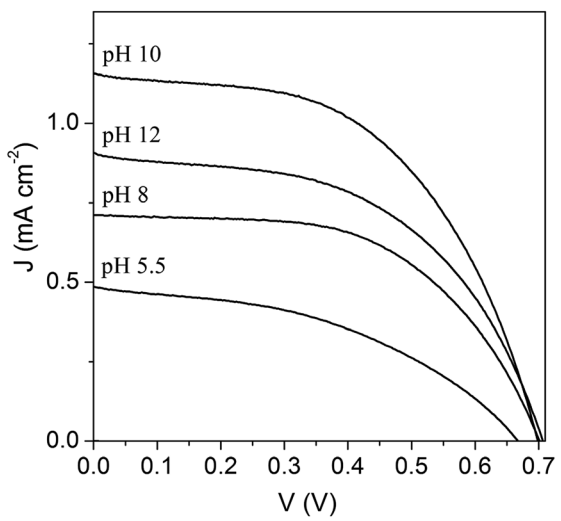

Fig. 6 Current–voltage curves for dye-sensitized solar cells prepared with ZnO on FTO as a function of the ZnO morphology.

Table 2 Characteristic parameters obtained from DSSCs prepared with ZnO powders obtained at different synthesis pH; the results represent an average of three sets of solar cells

pH	J_{SC} (mA cm^{-2})	V_{OC} (V)	FF	Efficiency (%)
5.5	0.48	0.66	0.44	0.14
8	0.71	0.70	0.56	0.27
10	1.16	0.70	0.53	0.42
12	0.90	0.70	0.52	0.33

It can be concluded that the short circuit current density correlates with the dye coverage, rather than with total surface area. If we assume that the injection efficiency does not depend

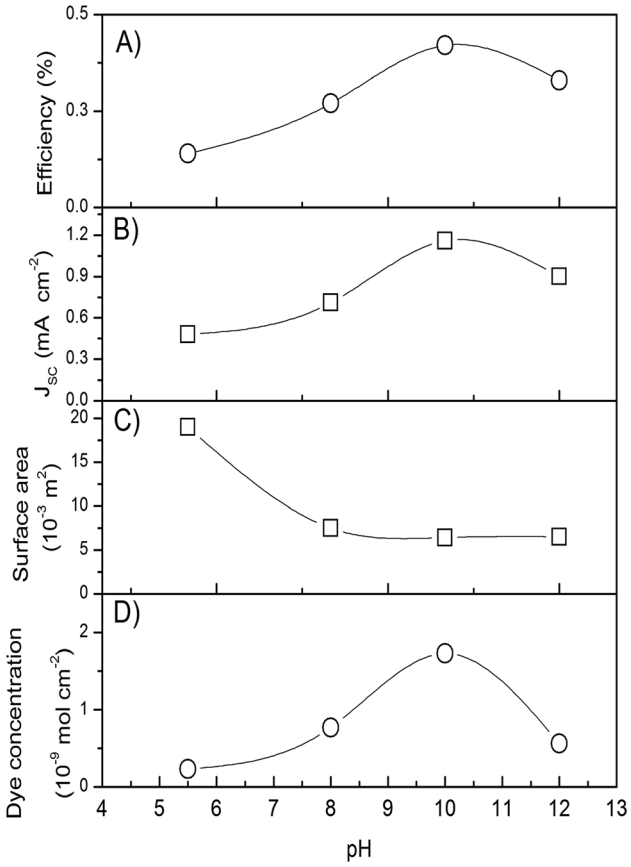

Fig. 7 (A) Efficiency, (B) short circuit current density, (C) total surface area, and (D) dye concentration as a function of the synthesis pH corresponding to different ZnO morphologies and textures.

on dye adsorption density, then the short-circuit current density is expected to be proportional to dye coverage. Fig. 7 illustrates the correlation between the short circuit current density and cell performance, and the surface area, dye coverage, and morphology and texture. It is clear from Fig. 7 that the solar cell efficiency is dominated by the dependence of the short circuit current density on the amount of dye adsorbed to the surface, and not to the total surface area. These tendencies were found in several repeat experiments, although in some sets of cells, the efficiency peaked at pH 8, with a slightly lower efficiency at pH 10. As shown in Fig. 5 (top), the texture coefficients corresponding to the {100} and {110} crystal forms for the ZnO powders are larger than 1 for the materials synthesized at pH 8 and pH 10. In particular, TC(110) is larger than 1 for pH 8 and pH 10, but smaller than 1 for pH 5.5 and pH 12, suggesting that dye adsorption is optimal at these surfaces, resulting in a relatively high coverage compared to other surfaces. On the other hand, the TC(002) values are largest at pH 5.5 and pH 12, indicating that these surfaces have a negative impact on dye adsorption and, hence, overall cell performance.

Fig. 8 shows the results from electrochemical impedance spectroscopy measurements. In Fig. 8A and B, the charge transfer resistance and chemical capacitance are shown *versus* the cell voltage on a semi-logarithmic scale. The chemical capacitance increases exponentially with cell voltage, indicating the presence of traps, while the charge transfer resistance corresponding to the recombination resistance decreases exponentially with cell voltage. These results are similar as commonly found for TiO_2-based DSSCs, and this behavior is typically associated to traps distributed exponentially in energy below the conduction band edge that dominate the electron transport and recombination kinetics. The following relationships can be defined:

$$C_{\mu} = C_{\mu,0} \exp\left(\frac{\alpha q V}{kT}\right) \quad (2)$$

$$R_{ct} = R_{ct,0} \exp\left(-\frac{\beta q V}{kT}\right) \quad (3)$$

If electron transport in the nanostructured ZnO film is trap-limited, the electron life time, τ, can be obtained according to the following relationship:

$$\tau = R_{ct} C_{\mu} \quad (4)$$

where $C_{\mu,0}$ and $R_{ct,0}$ are constants, k is the Boltzmann constant, T is the temperature and q is the elementary charge. The trap distribution parameter α can be related to the average depth of the traps below the conduction band, while β is an empirical parameter reflecting the non-linearity of the recombination kinetics.[54–56]

With the aid of eqn (2) and Fig. 8A, it can be observed that the values for α are the same for the different ZnO morphologies, indicating that the trap distribution is very similar with $\alpha = 0.11 \pm 0.01$. Similarly, with the aid of eqn (3) and Fig. 8B, the values for β are essentially the same for the different ZnO morphologies indicating that the recombination mechanism is the same for the different ZnO materials, characterized by $\beta = 0.51 \pm 0.06$. These values for the trap distribution and non-linear recombination parameters are in agreement with

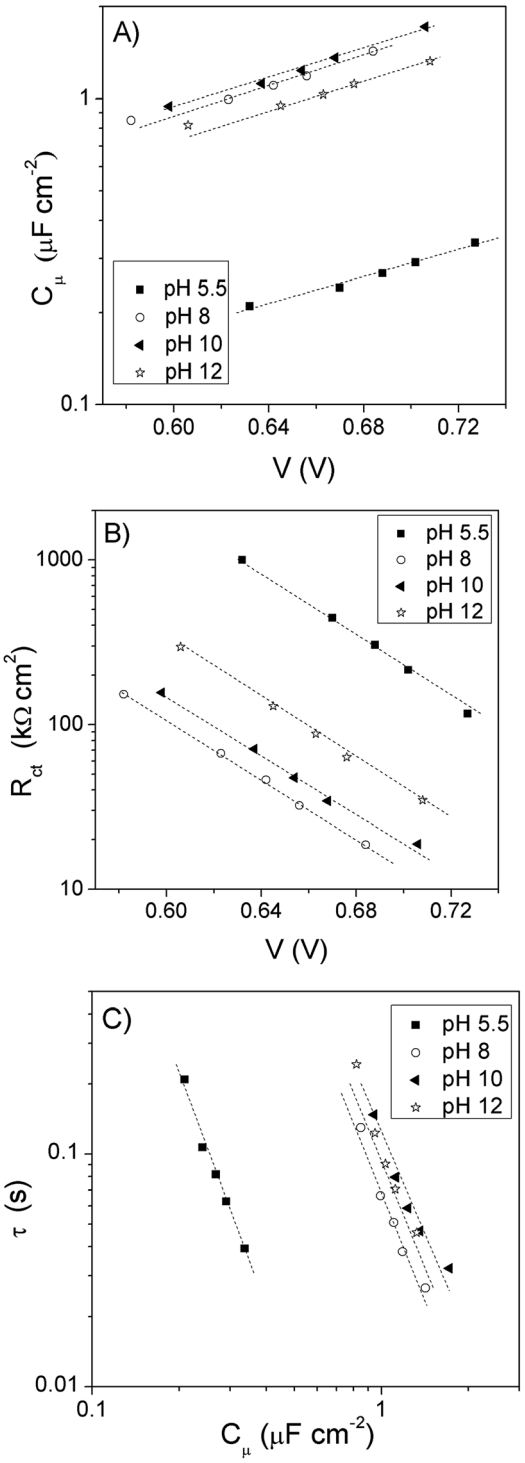

Fig. 8 Results of EIS measurements under open circuit conditions for different light intensities, resulting in different open circuit voltages, for DSSCs based on ZnO obtained at different pH values: (A) the chemical capacitance, and (B) charge transfer resistance *versus* voltage; (C) electron lifetime *versus* the chemical capacitance.

previous reports on ZnO-based DSSCs.[57–59] Assuming that the total trap density is the same for the different morphologies, the shift of the chemical capacitance *versus* voltage curves can be interpreted to be due to a shift of the conduction and valence band edges. The shift of the band edges can be determined by overlaying the chemical capacitance curves for each morphology as shown in the ESI.† Note that the shift of the recombination resistance *versus* voltage curves would also be partially related to a shift of the conduction and valence band edges. In order to determine the effect of the ZnO morphology on the recombination and transport characteristics it is useful to compare the materials at the same electron density in the ZnO nanostructured film.[60] Taking that the total trap density is the same for the different morphologies and with the experimental result that the trap distribution parameter is independent of ZnO morphology, this can be achieved by plotting the electron life time as a function of the chemical capacitance, which is shown in Fig. 8C. From Fig. 8C it can be concluded that the electron life-time decreases with increasing chemical capacitance, corresponding with increasing quasi-Fermi level, as is generally observed. An interesting observation is that the results overlay for the ZnO materials synthesized at pH 8, 10, and 12, while only for the material prepared at pH 5.5, the life time is markedly smaller at the same chemical capacitance due to a significantly smaller recombination resistance (see ESI†). Fig. 9 shows the shift of the band edges and the electron life-time at the same chemical capacitance as a function of synthesis pH, taking as a reference the sample prepared at pH 5.5. It can be observed that both parameters are very similar for the three higher pH values, while the result for pH 5.5 is markedly different. Note that the values of the life-time were obtained by extrapolation, and the error in these values is relatively large. The values for the electron life-time obtained in this study are on the same order of magnitude as reported in a previous study where nanocolumnar and nanoparticulate morphologies were compared.[55] From Fig. 9 it can be seen that the band edges for the three higher pH values are shifted to lower energy, which from a thermodynamic point of view would imply that the maximum open circuit potential attainable would decrease for these materials.

In general, the band edges of ZnO shift to higher energy when in contact with a solution at higher pH. Hence, it can be concluded that the band edge shift is not directly related to the synthesis solution pH, but rather to the basicity of the exposed surfaces. This can be expected since the preparation of the screen printing ZnO paste involves extensive treatment with a variety of organic solvents and rinsing with an aqueous acidic solution, thus erasing the synthesis solution pH memory at the interface. On the other hand, these results imply that the open circuit potential of the solar cells of the ZnO material prepared at pH 5.5 could be larger than for the other three pH values, which is not generally observed. This can be explained by the observation that the electron life-time for the ZnO material prepared at pH 5.5 is much smaller at the same electron density than for the other three materials; hence, the open circuit potential for the ZnO material prepared at pH 5.5 is smaller than thermodynamically possible due to faster recombination kinetics.[61]

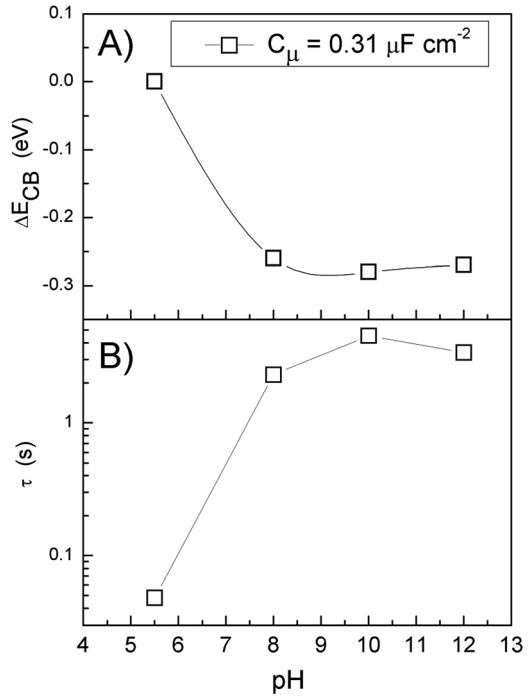

Fig. 9 (A) Shift of the conduction band edge, ΔE_{CB}; and (B) electron life time at the same chemical capacitance *versus* the synthesis pH of the ZnO nanomaterial.

4. Conclusions

Dye-sensitized solar cells have been prepared using ZnO nanoparticles with different morphologies synthesized by a sonochemical method with the aim to determine the effects of morphology and texture on the performance of DSSCs. The highest efficiency was found for solar cells prepared with ZnO synthesized at pH 10 related to a higher dye coverage, which was correlated with a stronger presence of the {001} and {110} crystal forms and weaker presence of the {002} crystal form. All ZnO materials were characterized by the same trap distribution parameter, and the electron life-time is essentially the same for the materials prepared at the three higher synthesis pH values (pH 8, 10, 12), while the life-time was significantly lower for the pH 5.5 material. As a consequence, the solar cell performance of the material prepared at pH 5.5 was inferior to the other three materials. However, the main factor determining cell performance was found to be the dye coverage, related to the differences in morphology and texture of the different ZnO materials studied in this work. These findings may provide useful information for the fabrication of high efficiency dye-sensitized solar cells.

Acknowledgements

CONACyT is gratefully acknowledged for funding under grants CB-2012-178510 and CB-2010-161767, and CONACyT/SENER

and IER-UNAM for funding through the Mexican Center for Innovation in Solar Energy (CeMIE-Sol), Project P-27. J. V. C. acknowledges PRODEP-SEP and VIEP-BUAP for financial support. We would like to acknowledge the invaluable help of Dora Huerta, José Bante, Leny Pinzón, Daniel Aguilar, and the National Laboratory for Nano and Biomaterials for the access to characterization equipments.

References

1 A. Hagfeldt, G. Boschloo, L. Sun, L. Kloo and H. Pettersson, *Chem. Rev.*, 2010, **110**, 6595–6663.
2 C. Bauer, G. Boschloo, E. Mukhtar and A. Hagfeldt, *J. Phys. Chem. B*, 2001, **105**, 5585–5588.
3 R. Katoh, A. Furube, A. V. Barzykin, H. Arakawa and M. Tachiya, *Coord. Chem. Rev.*, 2004, **248**, 1195–1213.
4 S. Zhang, X. Yang, C. Qin, Y. Numata and L. Han, *J. Mater. Chem. A*, 2014, **2**, 5167.
5 Q. F. Zhang, C. S. Dandeneau, X. Y. Zhou and G. Z. Cao, *Adv. Mater.*, 2009, **21**, 4087–4108.
6 D. C. Look, D. C. Reynolds, J. R. Sizelove, R. L. Jones, C. W. Litton, G. Cantwell and W. C. Harsch, *Solid State Commun.*, 1998, **105**, 399–401.
7 R. Katoh, A. Furube, T. Yoshihara, K. Hara, G. Fujihashi, S. Takano, S. Murata, H. Arakawa and M. Tachiya, *J. Phys. Chem. B*, 2004, **108**, 4818–4822.
8 J. Idígoras, G. Burdziński, J. Karolczak, J. Kubicki, G. Oskam, J. A. Anta and M. Ziółek, *J. Phys. Chem. C*, 2015, **119**, 3931–3944.
9 C. H. Seager and S. M. Myers, *J. Appl. Phys.*, 2003, **94**, 2888–2894.
10 T. Yoshida, J. Zhang, D. Komatsu, S. Sawatani, H. Minoura, T. Pauporté, D. Lincot, T. Oekermann, D. Schlettwein, H. Tada, D. Wöhrle, K. Funabiki, M. Matsui, H. Miura and H. Yanagi, *Adv. Funct. Mater.*, 2009, **19**, 17–43.
11 J. Sun, J. Bian, Y. Wang, S. Zhang, Y. Wang, Q. Feng, H. Liang and G. Du, *Thin Solid Films*, 2012, **521**, 253–256.
12 S. Zhu, X. Chen, F. Zuo, M. Jiang, Z. Zhou and D. Hui, *J. Solid State Chem.*, 2013, **197**, 69–74.
13 S. Promnimit, S. Baruah, U. Lamdu and J. Dutta, *J. Nano Res.*, 2012, **21**, 57–63.
14 Y. Zhou, D. Li, X. Zhang, J. Chen and S. Zhang, *Appl. Surf. Sci.*, 2012, **261**, 759–763.
15 L. Chen, X. Li, L. Qu, C. Gao, Y. Wang, F. Teng, Z. Zhang, X. Pan and E. Xie, *J. Alloys Compd.*, 2014, **586**, 766–772.
16 P. Rai, R. Khan, R. Ahmad, Y.-B. Hahn, I.-H. Lee and Y.-T. Yu, *Curr. Appl. Phys.*, 2013, **13**, 1769–1773.
17 T. Borkar, W. Seok, J. Yeon, N. D. Shepherd and R. Banerjee, *Mater. Res. Bull.*, 2012, **47**, 2756–2759.
18 A. J. Tzou, K. F. Chien, H. Y. Lai, J. T. Ku, L. Lee, W. C. Fan and W. C. Chou, *J. Cryst. Growth*, 2013, **378**, 466–469.
19 X. Zhang, S. Ma, F. Li, F. Yang, J. Liu and Q. Zhao, *J. Alloys Compd.*, 2013, **574**, 149–154.
20 Y. Linn, J. Yang and Y. Meng, *Ceram. Int.*, 2013, **39**, 5049–5052.
21 F. I. Lizama-Tzec, M. A. Aguilar-Frutis, G. Rodríguez-Gattorno and G. Oskam, *J. New Mater. Electrochem. Syst.*, 2013, **215**, 209–215.
22 T. Thongtem, A. Phuruangrat and S. Thongtem, *Curr. Appl. Phys.*, 2009, **9**, S197–S200.
23 N. Morales-Flores, R. Galeazzi, E. Rosendo, T. Díaz, S. Velumani and U. Pal, *Advances in Nano Research*, 2013, **1**, 59–70.
24 F. Xu, Y. Lu, Y. Xie and Y. Liu, *Mater. Des.*, 2009, **30**, 1704–1711.
25 M. Law, L. E. Greene, J. C. Johnson, R. Saykally and P. Yang, *Nat. Mater.*, 2005, **4**, 455–459.
26 M. Hosni, Y. Kusumawati, S. Farhat, N. Jouini and T. Pauporté, *J. Phys. Chem. C*, 2014, **118**, 16791–16798.
27 T. Toyoda, T. Sano, J. Nakajima, S. Doi and S. Fukumoto, *J. Photochem. Photobiol., A*, 2004, **164**, 203–207.
28 K. Kalyanasundaram, *Dye-Sensitized Solar Cells*, EPFL Press, 2010.
29 F. Fabregat-Santiago, G. Garcia-Belmonte, I. Mora-Seró and J. Bisquert, *Phys. Chem. Chem. Phys.*, 2011, **13**, 9083–9118.
30 R. Escalante-Quijano, R. García-Rodríguez, B. E. Heredia-Cervera, N. Gómez-Ortíz, J. Villanueva-Cab and G. Oskam, *Energy and Environment Focus*, 2014, **2**, 1–7.
31 H. Zhang, D. Yang, Y. Ji, X. Ma, J. Xu and D. Que, *J. Phys. Chem. B*, 2004, **108**, 3–6.
32 J. D. H. Donnay and D. Harker, *Am. Mineral.*, 1937, **22**, 446.
33 R. Boppella, K. Anjaneyulu, B. Pratyay and V. Manorama Sunkara, *J. Phys. Chem. C*, 2013, **117**, 4597–4605.
34 L. Wen-Jun, S. Er-Wei, Z. Wei-Zhuo and Y. Zhi-Wen, *J. Cryst. Growth*, 1999, **203**, 186–196.
35 R. Wahab, K. Young-Soon and S. Hyung-Shik, *Mater. Trans.*, 2009, **50**, 2092–2097.
36 P. Santiago and U. Pal, *J. Phys. Chem. B*, 2005, **109**, 15317–15321.
37 W. Huang, J. Jia, X. Zhou and Y. Lin, *Mater. Chem. Phys.*, 2010, **123**, 104–108.
38 A. Huang and J. Caro, *J. Cryst. Growth*, 2010, **312**, 2977–2982.
39 A. Huang and J. Caro, *J. Cryst. Growth*, 2010, **312**, 947–952.
40 B. Ludi and M. Niederberger, *Dalton Trans.*, 2013, **42**, 12554–12568.
41 E. Palacios-Lidón, B. Pérez-García, P. Vennéguès, J. Colchero, V. Muñoz-Sanjosé and J. Zúñiga-Pérez, *Nanotechnology*, 2009, **20**, 065701.
42 N. J. Nicholas, G. V. Franks and W. A. Ducker, *Langmuir*, 2012, **28**, 5633–5641.
43 J. M. Azpiroz and F. De Angelis, *J. Phys. Chem. A*, 2014, **118**, 5885–5893.
44 R. Gonzáles-Moreno, P. L. Cook, I. Zegkinoglou, X. Liu, P. S. Johnson, W. Yang, R. E. Ruther, R. J. Hamers, F. J. Himpsel, J. E. Ortega and C. Rogero, *J. Phys. Chem. C*, 2011, **115**, 18195–18201.
45 E. Palacios-Lidón, D. F. Pickup, P. S. Johnson, R. E. Ruther, R. J. Hamers, J. Colchero, F. J. Himpsel, J. E. Ortega and C. Rogero, *J. Phys. Chem. C*, 2013, **117**, 18414–18422.
46 J. Chang, R. Ahmed, H. Wang, H. Liu, R. Li, P. Wang and E. R. Waclawik, *J. Phys. Chem. C*, 2013, **117**, 13836–13844.
47 R. E. Sherriff, D. C. Reynolds, D. C. Look, B. Jogai, J. E. Hoelscher, T. C. Collins, G. Cantwell and W. C. Harsch, *J. Appl. Phys.*, 2000, **88**, 3454–3457.

48 H. Sasaki, H. Kato, F. Izumida, H. Endo, K. Maeda, M. Ikeda, Y. Kashiwaba and I. Niikura, *Phys. Status Solidi*, 2006, **3**, 1034–1037.
49 I. Beinik, M. Kratzer, A. Wachauer, L. Wang, R. T. Lechner, C. Teichert, C. Motz, W. Anwand, G. Brauer, X. Y. Chen, X. Y. Hsu and A. B. Djurišić, *J. Appl. Phys.*, 2011, **110**, 052005.
50 J. G. Ok, J. Y. Lee, H. W. Baac, S. H. Tawfick, L. J. Guo and A. J. Hart, *ACS Appl. Mater. Interfaces*, 2014, **6**, 874–881.
51 Y. Wu, N. Yu, D. Liu, Y. He, Y. Liu, H. Liang and G. Du, *Appl. Surf. Sci.*, 2013, **265**, 176–179.
52 Z.-S. Wang, H. Kawauchi, T. Kashima and H. Arakawa, *Coord. Chem. Rev.*, 2004, **248**, 1381–1389.
53 M. Ney Henrique, A. Domínguez, T. Frauenheim and A. Luisa da Rosa, *Phys. Chem. Chem. Phys.*, 2012, **14**, 15445–15451.
54 J. Bisquert and I. Mora-Seró, *J. Phys. Chem. Lett.*, 2010, **1**, 450–456.
55 A. G. Vega-Poot, M. Macias-Montero, A. Barranco, A. Borras, A. R. Gonzalez-Elipe, G. Oskam and J. A. Anta, *Energy and Environment Focus*, 2013, **2**, 270–276.
56 J. Villanueva-Cab, H. Wang, G. Oskam and L. M. Peter, *J. Phys. Chem. Lett.*, 2010, **1**, 748–751.
57 R. Agosta, R. Giannuzzi, L. De Marco, M. Manca, M. R. Belviso, P. D. Cozzoli and G. Gigli, *J. Phys. Chem. C*, 2013, **117**, 2574–2583.
58 R. Tena-Zaera, J. Elias, C. Lévy-Clément, C. Bekeny, T. Voss, I. Mora-Seró and J. Bisquert, *J. Phys. Chem. C*, 2008, **112**, 16318–16323.
59 J. A. Anta, E. Guillén and R. Tena-Zaera, *J. Phys. Chem. C*, 2012, **116**, 11413–11425.
60 E. Guillén, L. M. Peter and J. A. Anta, *J. Phys. Chem. C*, 2011, **115**, 22622–22632.
61 F. Fabregat-Santiago, J. Bisquert, G. Garcia-Belmonte, G. Boschloo and A. Hagfeldt, *Sol. Energy Mater. Sol. Cells*, 2005, **87**, 117–131.